

On the Boundary Layers of the Bidirectional Vortex

Joshua W. Batterson* and Joseph Majdalani†
 University of Tennessee Space Institute, Tullahoma, TN 37388

To complement former studies of the bidirectional vortex, our principal focus here is to resolve the viscous boundary layers forming in both the axial and radial directions at the sidewall of a vortex chamber. The analysis is initiated by the formulation of the laminar boundary layer equations via an order of magnitude reduction of the incompressible Navier-Stokes equations at the wall. Next, asymptotic concepts are applied to linearize and rigorously truncate the governing equations, thus converting them, when possible, from PDEs to manageable ODEs. Scaling transformations are then applied to resolve the rapid changes near the sidewall. Due to the nature of the outer solutions, additional transformations of the dependent variables are undertaken to permit securing the problem's multiple boundary conditions. After some algebra and matched-asymptotic expansions, we recover nearly identical boundary layer structures in all three orthogonal directions: the axial and radial components presented here, and the wall-tangential boundary layer formulated previously. This behavior is not surprising given that the resultant velocity is dominated by its tangential component and that the tangential boundary layer is axially invariant. This forces the axial layer to remain uniform in the streamwise direction. Corroborating assumptions include an axially independent pressure distribution and consistency in the asymptotic assumptions made, the linearization techniques, and the governing equations that apply to all three cases. We remark that although curvature terms are retained initially, they are found to be so small that the problem is reducible to the case of two-dimensional layer analysis. It can be seen that all viscous corrections at the wall are strongly dependent on the vortex Reynolds number, V . With the newly obtained solutions, essential flow characteristics, such as pressure, vorticity, swirling intensity, and wall shear stresses, are evaluated and discussed. We find the axial and tangential boundary layers to be of the same size, approximately twice the thickness of the radial layer.

Nomenclature

| | |
|--------------|---|
| a | = chamber radius |
| A_i | = inlet area |
| b | = chamber outlet radius |
| l | = chamber aspect ratio, L/a |
| \bar{p} | = normalized pressure, $\bar{p}/(\rho U^2)$ |
| \bar{Q}_i | = inlet volumetric flow rate |
| Q_i | = normalized volumetric flow rate, $\bar{Q}_i/(Ua^2) = \sigma^{-1}$ |
| Re | = injection Reynolds number, $Ua/\nu = 1/\varepsilon$ |
| r, z | = normalized radial or axial coordinates, $\bar{r}/a, \bar{z}/a$ |
| s | = scaled transformation variable, $(\pi - \eta)/\delta$ |
| S | = swirl number, $\pi ab/A_i = \pi\beta\sigma$ |
| \mathbf{u} | = normalized velocity $(\bar{u}_r, \bar{u}_z, \bar{u}_\theta)/U$ |
| u_θ | = normalized swirl/spin/tangential velocity, \bar{u}_θ/U |
| U | = average inflow velocity in the tangential direction, $\bar{u}_\theta(a, L)$ |
| V | = vortex Reynolds number, $Q_i Re(a/L) = (\varepsilon\sigma l)^{-1}$ |

*Graduate Research Assistant, Department of Mechanical, Aerospace and Biomedical Engineering. Member AIAA.

†Jack D. Whitfield Professor of High Speed Flows, Department of Mechanical, Aerospace and Biomedical Engineering. Member AIAA. Fellow ASME.

Greek

| | |
|---------------|--|
| α | = constant, $\frac{1}{6}\pi^2 - 1 \approx 0.644934$ |
| β | = normalized outlet radius, b/a |
| δ | = η -rescaled layer |
| δ_w | = wall boundary layer thickness, $\bar{\delta}_w/a$ |
| ε | = perturbation parameter, $1/Re = \nu/(Ua)$ |
| η | = transformed variable, πr^2 |
| κ | = inflow parameter, $Q_i/(2\pi l) = (2\pi\sigma l)^{-1}$ |
| ν | = kinematic viscosity, μ/ρ |
| ρ | = density |
| σ | = modified swirl number, $Q_i^{-1} = S/(\pi\beta)$ |

Subscripts

| | |
|----------|-----------------------|
| i | = inlet property |
| r | = radial component |
| z | = axial component |
| θ | = azimuthal component |

Superscripts

| | |
|------|---|
| | = overbars denote dimensional variables |
| o | = outer (inviscid) solution |

I. Introduction

CHARACTERIZATION of unidirectional vortex flows has remained a central topic of interest since its earliest model was released by Rankine¹ in 1858. Other notable advancements may be ascribed to Lamb-Oseen,² Burgers-Rott,³ Batchelor,⁴ and others. These basic flows remain valuable tools in modeling natural atmospheric and stellar phenomena.^{5,6} For example, the Rankine vortex is still used as a crude approximation for describing the bulk motion of hurricanes and other large, atmospheric, swirl-dominated patterns. Jupiter's Great Red Spot is also regarded as a Rankine type vortex.⁷ Lamb-Oseen and Burgers-Rott vortices are closely related in that they can both be defined in terms of a Gaussian function.⁸ As shown by Batterson *et al.*,⁹ they become identical when suitably normalized, and both can be applied to localized atmospheric swirling flows such as tornados, dust devils, and water spouts. Being relevant to a variety of phenomenological applications, interest in their behavior continues to receive attention. The reader is referred in this regard to recent investigations by Alekseenko *et al.*,¹⁰ Eloy and Le Dizès,⁸ Schmid and Rossi,¹¹ Olendraru and Sellier,¹² Pérez-Saborid *et al.*,¹³ and others. Included among its pertinent applications, the Lamb-Oseen solution appears to be a viable model for trailing vortex streaks produced by lifting bodies and other such vortices that dissipate with time as a result of shear. These, however, are restricted to unidirectional vortex distributions.

A glimpse at bidirectional motion may be caught in Sullivan's 1959 solution of an external two-cell vortex.¹⁴ Sullivan characterizes the swirl velocity in terms of integral functions and mates this profile with both axial and radial components. Common to all of these models is the existence of two fundamental regions: a forced vortex forming around the axis of rotation and a free vortex that is essentially irrotational. While the free vortex is inviscid, the character of the forced vortex is dominated by viscous stresses. In these models, both the forced vortex diameter and maximum swirl velocity diminish with successive increases in viscosity (see Vastistas *et al.*¹⁵⁻¹⁷).

In the context of bidirectional flow, Bloor and Ingham¹⁸ have analyzed the flow in cyclonic separators assuming a conical geometry that incorporates a vortex finder. Their solution, albeit inviscid, may be considered a milestone achievement in advancing the theory of confined swirl dominated flows. Bloor and Ingham's motivation was industry driven, specifically geared toward cyclonic devices (see Fig. 1). These are widely used in the petrochemical, mineral, and powder processing industries. As for its application to rocketry, Chiaverini, Knuth and co-workers¹⁹⁻²¹ may be said to have truly pioneered the implementation of bidirectional swirl technology in the development of liquid rocket thrust engines, including the self-cooling Vortex Combustion Cold-Wall Chamber (VCCWC).

The exact solution to Euler's equations in reference to the VCCWC flowfield was discovered by Vyas and Majdalani²² directly from first principles. It was further extended to spherical geometry by Majdalani and Rienstra.²³

Their exact solution resembled Bloor and Ingham's in exhibiting a singularity at the centerline. Immediately thereafter, viscous corrections were derived to overcome the swirl velocity's singularity at the origin²⁴ and later, the no slip at the sidewall in the tangential direction.²⁵ Thus, with the exception of Bloor and Ingham,¹⁸ no other bidirectional vortex model has been advanced despite its relevance to both the propulsion and particle separation industries. For this reason, the present article is aimed at developing an improved representation of the bidirectional vortex that will secure the sidewall boundary layers in all three spatial directions: axial, radial, and tangential. The accurate treatment of the problem's boundary layers will be essential in predicting the potential for roll torques. These can play an important role in the design of guidance equipment.

To engage the treatment of boundary layers at the confining sidewall, standard asymptotic techniques will be applied to the previously untreated radial and axial velocity profiles. These will enable us to construct uniformly valid, matched-asymptotic approximations for the two remaining components of the velocity. We initiate the analysis by reducing the Navier-Stokes equations to recover Prandtl's boundary layer equations.²⁶ We then follow Vyas and Majdalani²⁵ and Conlisk²⁷ in seeking asymptotic simplifications that ultimately lead to the desired solutions. As a corollary to the velocity treatment, we derive new expressions for the pressure distribution, shear stresses, vorticity, swirling intensity, and other characteristics of the boundary layers.

II. Mathematical Formulation

The mathematical model, nomenclature, normalization, and coordinate system follow those employed by Vyas and Majdalani²⁵ (see Fig 2). We recognize that the decoupled axial and radial profiles are characterized by different velocity and length scales than those originally used by Vyas and Majdalani. Renormalization with respect to characteristic parameters in the longitudinal direction can be shown to result in the same solution. To remain consistent throughout the problem, the original normalization is utilized here. Accordingly, the spatial coordinates are referenced to the radius a and the velocities to the average wall tangential injection speed U . As usual, the flow is assumed to be axisymmetric and steady.

A. Axial Corrections

The axial boundary layer equations can be derived according to Prandtl's order of magnitude reduction applied to the cylindrical Navier-Stokes equations.²⁶ These are obtained by truncating at $O(\delta)$, where $\varepsilon \sim \delta^2$, $r \sim \delta$, and $u_z \sim z \sim O(1)$. Furthermore, we take flows parallel to the surface (or tangent in the cylindrical case) to be of order unity (see Tetervin²⁸). The boundary layer equation can thus be manipulated and simplified. In nondimensional form, it can be written as

$$u_r \frac{\partial u_z}{\partial r} + u_z \frac{\partial u_z}{\partial z} = -\frac{\partial p}{\partial z} + \varepsilon \left(\frac{\partial^2 u_z}{\partial r^2} + \frac{1}{r} \frac{\partial u_z}{\partial r} \right) \quad (1)$$

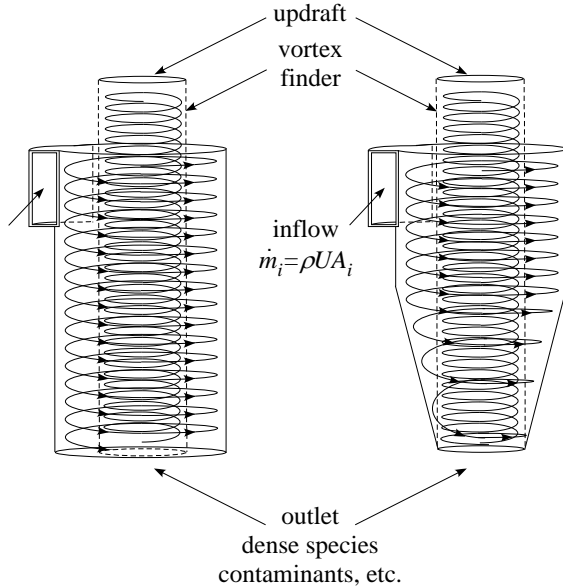


Figure 1. Sketch of cylindrical (left) and conical (right) cyclone separators with heavy uses in industry.

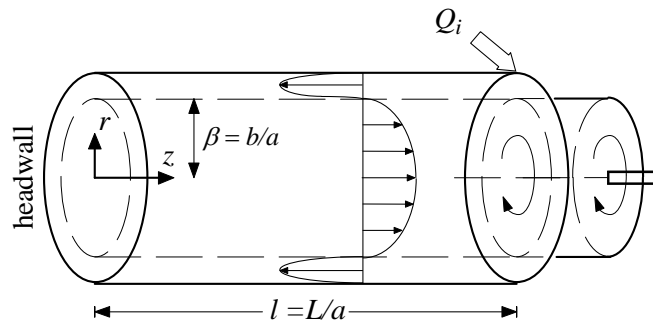


Figure 2. Idealized chamber geometry and coordinate system.

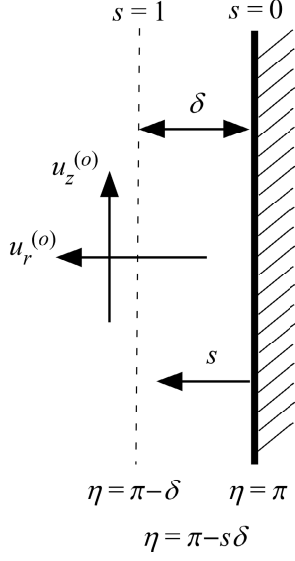


Figure 3. Coordinate transformations in the sidewall boundary layer region.

with the conditions

$$\begin{cases} u_z(1, z) = 0 \\ \lim_{r \rightarrow 0} u_z(r, z) = u_z^{(o)} \end{cases} \quad (2)$$

Here $u_z^{(o)}$ represents the outer solution that must be recovered as $u_z(r, z)$ leaves the near wall region. To begin, the pressure gradient term is extracted from the inviscid solution, $\partial p / \partial z = -4\pi^2 \kappa^2 z$. Knowing the inflow parameter κ to be small, we can assume the pressure gradient to be so small that it can be ignored. Later we find that the pressure gradient naturally disappears. Another simplification can be made after Conlisk.²⁷ Recognizing that radial gradients far outweigh the axial ones, $\partial / \partial r \gg \partial / \partial z$, derivatives with respect to the axial coordinate are neglected. This assumption is further confirmed by outer axial pressure and velocity gradients being very small in comparison to the radial ones. Naturally, the outer radial velocity may be used to approximate the variable coefficient in the boundary layer equation. Applying these assumptions to Eq. (1) delivers the compact form

$$\varepsilon \frac{1}{r} \frac{\partial}{\partial r} \left(r \frac{\partial u_z}{\partial r} \right) + \frac{\kappa}{r} \sin(\pi r^2) \frac{\partial u_z}{\partial r} = -4\pi^2 \kappa^2 z \quad (3)$$

At this juncture, a useful variable transformation employed by Vyas and Majdalani²⁵ may be implemented. Letting $\eta = \pi r^2$ and $\partial / \partial r = 2\pi r \cdot \partial / \partial \eta$, substitution into Eq. (3) leads to

$$\varepsilon \left(\frac{\partial^2 u_z}{\partial \eta^2} + \frac{1}{\eta} \frac{\partial u_z}{\partial \eta} \right) + \frac{\kappa}{2\eta} \sin(\eta) \frac{\partial u_z}{\partial \eta} = -\frac{\pi \kappa^2 z}{\eta} \quad (4)$$

In order to more easily confront the rapid changes near the wall we seek a scaling transformation that will be appropriate in the boundary layer region (see Fig. 3). Given that as $r \rightarrow 1, \eta \rightarrow \pi$, we select the stretched coordinate transformation

$$s = \frac{\pi - \eta}{\delta}; \quad \eta = \pi - s\delta \quad (5)$$

We thus arrive at

$$\frac{\varepsilon}{\delta^2} \left(\frac{\partial^2 u_z}{\partial s^2} - \frac{\delta}{\pi - s\delta} \frac{\partial u_z}{\partial s} \right) - \frac{\kappa}{2\delta(\pi - s\delta)} \sin(\pi - s\delta) \frac{\partial u_z}{\partial s} = -\frac{\pi \kappa^2 z}{\pi - s\delta} \quad (6)$$

Next, we expand the sine term

$$\begin{aligned} -\frac{\kappa}{2\delta(\pi - s\delta)} \sin(\pi - s\delta) &\approx -\frac{\kappa}{2\delta(\pi - s\delta)} \left[\pi - s\delta - \frac{1}{6}(\pi - s\delta)^3 \right] \\ &= -\frac{\kappa}{2\delta} \left[1 - \frac{1}{6}(\pi - s\delta)^2 \right] \approx \frac{\kappa}{2\delta} \left(\frac{1}{6}\pi^2 - 1 \right) \end{aligned} \quad (7)$$

Upon substitution into Eq. (6), we obtain the linearized form of the equation,

$$\frac{\varepsilon}{\delta^2} \left(\frac{\partial^2 u_z}{\partial s^2} - \frac{\delta}{\pi - s\delta} \frac{\partial u_z}{\partial s} \right) + \frac{\kappa}{2\delta} \left(\frac{1}{6}\pi^2 - 1 \right) \frac{\partial u_z}{\partial s} = -\frac{\pi \kappa^2 z}{\pi - s\delta} \quad (8)$$

Then, in an effort to counterbalance the key terms above, we take the distinguished limit to be $\delta \approx \varepsilon / \kappa$. This enables us to revisit Eq. (8) and eliminate the inhomogeneous and curvature terms at order ε . We obtain

$$\frac{\partial^2 u_z}{\partial s^2} + \frac{\alpha}{2} \frac{\partial u_z}{\partial s} = 0; \alpha \equiv \frac{1}{6} \pi^2 - 1 \quad (9)$$

with the new boundary conditions

$$\begin{cases} u_z(0, z) = 0 \\ \lim_{s \rightarrow \infty} u_z(s, z) = u_z^{(o)} \end{cases} \quad (10)$$

Upon careful examination of the boundary conditions on the inner solution, we find it necessary to apply a transformation of the dependent variable, namely $u_z = \xi_z(s, z) \pi z \cos(\pi - 2\pi s V^{-1})$; $V \gg 1$. In doing so, a constant limit is placed on ξ_z rather than the variable condition that plagues Eq. (10). To see this effect, we first expand the derivatives and dismiss terms of order V^{-1} . We collect

$$\begin{cases} \frac{\partial u_z}{\partial s} = -\pi z \cos\left(2\pi \frac{s}{V}\right) \frac{\partial \xi_z}{\partial s} + 2\pi^2 \frac{z}{V} \sin\left(2\pi \frac{s}{V}\right) \xi_z \approx -\pi z \cos\left(2\pi \frac{s}{V}\right) \frac{\partial \xi_z}{\partial s} \\ \frac{\partial^2 u_z}{\partial s^2} = -\pi z \cos\left(2\pi \frac{s}{V}\right) \frac{\partial^2 \xi_z}{\partial s^2} + 4\pi^2 \frac{z}{V} \sin\left(2\pi \frac{s}{V}\right) \frac{\partial \xi_z}{\partial s} + 4\pi^3 \frac{z}{V^2} \cos\left(2\pi \frac{s}{V}\right) \xi_z \approx -\pi z \cos\left(2\pi \frac{s}{V}\right) \frac{\partial^2 \xi_z}{\partial s^2} \end{cases} \quad (11)$$

These turn Eq. (9) into

$$-\pi z \cos\left(2\pi \frac{s}{V}\right) \frac{\partial^2 \xi_z}{\partial s^2} - \frac{\alpha}{2} \pi z \cos\left(2\pi \frac{s}{V}\right) \frac{\partial \xi_z}{\partial s} = 0 \quad \text{or} \quad \frac{\partial^2 \xi_z}{\partial s^2} - \frac{\alpha}{2} \frac{\partial \xi_z}{\partial s} = 0 \quad (12)$$

As for the boundary conditions, they become

$$\begin{cases} \xi_z(0, z) = 0 \\ \lim_{s \rightarrow \infty} \xi_z(s, z) = \xi_z^{(o)} = 2\kappa \end{cases} \quad (13)$$

Having identified a second order PDE with sufficient auxiliary conditions, partial integration may be pursued to retrieve

$$\xi_z(s, z) = 2\kappa \left[1 - \exp\left(-\frac{1}{2} \alpha s\right) \right] \quad (14)$$

Rewriting Eq. (14) in terms of the original variables, a viscous-corrected axial velocity is realized. This solution satisfies the no slip requirement and reproduces the outer solution when sufficiently removed from the sidewall. It is given by

$$u_z(r, z) = 2\pi\kappa z \cos(\pi r^2) \left[1 - e^{-\frac{1}{4}(\frac{1}{6}\pi^2 - 1)V(1-r^2)} \right] = u_z^{(o)} \left[1 - e^{-\frac{1}{4}(\frac{1}{6}\pi^2 - 1)V(1-r^2)} \right] \quad (15)$$

Here $V = 2\pi\kappa/\varepsilon$ is the same vortex Reynolds number first discovered by Vyas, Majdalani and Chiaverini.²⁴ Note the symmetry between the axial and the tangential velocity corrections near the wall.

B. Radial Corrections

Corrections of this order are typically disregarded when the inviscid velocity vanishes at the wall (see Culick²⁹ or Majdalani and Saad³⁰). Although as in the case here, we opt to revisit the radial momentum equation without sacrificing the higher order viscous terms. This effort is pursued for the sake of consistency with the axial and tangential solutions obtained previously. As we later describe in detail, we find viscosity to have a tempering effect on the slope of the radial velocity profile near the wall. As before, our starting point is the reduced radial momentum equation in which, contrary to its axial counterpart, second order terms are retained to avoid a meaningless outcome. The analysis begins with

$$\varepsilon \left(\frac{\partial^2 u_r}{\partial r^2} + \frac{1}{r} \frac{\partial u_r}{\partial r} - \frac{u_r}{r^2} \right) - u_r \frac{\partial u_r}{\partial r} + \frac{u_\theta^2}{r} - u_z \frac{\partial u_r}{\partial z} = \frac{\partial p}{\partial r} \quad (16)$$

subject to

$$\begin{cases} u_r(1) = 0 \\ \lim_{r \rightarrow 0} u_r(r) = u_r^{(o)} \end{cases} \quad (17)$$

The next step is to ignore axial derivatives by insisting that radial effects are more significant. As for the pressure gradient, it is calculated from the inviscid solution obtained by Vyas and Majdalani,²² specifically

$$\frac{\partial p}{\partial r} = \frac{\kappa^2}{r^3} \sin^2(\pi r^2) \left[1 - 2\kappa\pi r^3 \cot(\pi r^2) \right] + \frac{u_\theta^2}{r} \quad (18)$$

When Eq. (18) is substituted back into Eq. (16), the u_θ^2/r terms cancel. What remains on the right-hand-side may be recognized to be $O(\kappa^2)$ near the wall. As before, the inviscid solution may be injected into the coefficients of the boundary layer equation. These operations turn Eq. (16) into

$$\varepsilon \left[\frac{1}{r} \frac{d}{dr} \left(r \frac{du_r}{dr} \right) + \frac{\kappa}{r^3} \sin(\pi r^2) \right] + \frac{\kappa}{r} \sin(\pi r^2) \frac{du_r}{dr} = O(\kappa^2) \quad (19)$$

The standard transformation $\eta = \pi r^2$ may now be used. It yields

$$\varepsilon \left[\frac{d^2 u_r}{d\eta^2} + \frac{1}{\eta} \frac{du_r}{d\eta} + \frac{\kappa\sqrt{\pi}}{4\eta^{5/2}} \sin(\eta) \right] + \frac{\kappa}{2\eta} \sin(\eta) \frac{du_r}{d\eta} = O(\kappa^2) \quad (20)$$

To magnify the region of nonuniformity, stretching of the radial coordinate near the wall is required. Using the slow variable $s = (\pi - \eta)/\delta$, one may substitute into Eq. (20) and expand the sinusoidal terms. One gets

$$\frac{\varepsilon}{\delta^2} \left[\frac{d^2 u_r}{ds^2} - \frac{\delta}{\pi - s\delta} \frac{du_r}{ds} + \frac{\delta^2 \kappa \sqrt{\pi}}{4(\pi - s\delta)^{5/2}} \sin(\pi - s\delta) \right] + \frac{\kappa}{2\delta} \left(\frac{\pi^2}{6} - 1 \right) \frac{du_r}{ds} = \frac{1}{4\pi(\pi - s\delta)} O(\kappa^2) \quad (21)$$

where a distinguished limit of $\delta \approx \varepsilon/\kappa$ is rediscovered. Without loss in generality, we insert $\delta = \varepsilon/\kappa$ into Eq. (21) and drop all terms of higher order. A simple equation ensues, namely,

$$\frac{d^2 u_r}{ds^2} + \frac{\alpha}{2} \frac{du_r}{ds} = 0 \quad \text{with} \quad \begin{cases} u_r(0) = 0 \\ \lim_{s \rightarrow \infty} u_r(s) = u_r^{(o)} \end{cases} \quad (22)$$

To overcome the difficulty of equating a constant limit to a variable outer solution, we introduce a transformation of the dependent variable, $\xi_r = ru_r/\sin(\pi r^2)$. Subsequent substitution into Eq. (22) leads to

$$\begin{cases} \frac{\partial u_r}{\partial s} = \left[\frac{2\pi \cos \varphi}{V\sqrt{1-2sV^{-1}}} + \frac{\sin \varphi}{V(1-2sV^{-1})^{3/2}} \right] \xi_r + \frac{\sin \varphi}{\sqrt{1-2sV^{-1}}} \frac{\partial \xi_r}{\partial s} \approx \frac{\sin \varphi}{\sqrt{1-2sV^{-1}}} \frac{\partial \xi_r}{\partial s}; \quad \varphi \equiv 2\pi sV^{-1} \\ \frac{\partial^2 u_r}{\partial s^2} = \left[\frac{4\pi \cos \varphi}{V^2(1-2sV^{-1})^{3/2}} + \frac{3\sin \varphi}{V^2(1-2sV^{-1})^{5/2}} - \frac{4\pi^2 \sin \varphi}{V^2\sqrt{1-2sV^{-1}}} \right] \xi_r \\ + 2 \left[\frac{2\pi \cos \varphi}{V\sqrt{1-2sV^{-1}}} + \frac{\sin \varphi}{V(1-2sV^{-1})^{3/2}} \right] \frac{\partial \xi_r}{\partial s} + \frac{\sin \varphi}{\sqrt{1-2sV^{-1}}} \frac{\partial^2 \xi_r}{\partial s^2} \approx \frac{\sin \varphi}{\sqrt{1-2sV^{-1}}} \frac{\partial^2 \xi_r}{\partial s^2} \end{cases} \quad (23)$$

These derivatives change Eq. (22) into

$$\frac{d^2 \xi_r}{ds^2} + \alpha \frac{d\xi_r}{ds} = 0 \quad \text{with} \quad \begin{cases} \xi_r(0) = 0 \\ \lim_{s \rightarrow \infty} \xi_r(s) = -\kappa \end{cases} \quad (24)$$

Forthwith, a solution can be achieved in terms of

$$\xi_r(s) = -\kappa \left[1 - \exp(-\alpha s) \right] \quad (25)$$

or, in terms of original variables, we extract

$$u_r(r, z) = -\frac{\kappa}{r} \sin(\pi r^2) \left[1 - e^{-\frac{1}{2}(\frac{\pi^2}{6} - 1)V(1-r^2)} \right] = u_r^{(o)} \left[1 - e^{-\frac{1}{2}(\frac{\pi^2}{6} - 1)V(1-r^2)} \right] \quad (26)$$

Note that the viscous correction multiplier on the right-hand-side of Eq. (26) is similar in form to that arising in the axial velocity. The difference here is the factor of $1/2$ instead of $1/4$ that appears in the exponential damping argument.

III. Results and Discussion

A. Axial Velocity Profile

The modified axial velocity captures the effects of fluid friction near the wall. It rectifies the deficiency in the inviscid solution by permitting the satisfaction of the no-slip condition. Figure 4 illustrates the behavior of the new solution with respect to two key parameters: position and vortex Reynolds number. Since the original solution was linearly dependent on the axial coordinate, we continue to observe larger axial velocities at progressively larger axial distances. As with the tangential velocity, we recognize a strong dependence on the vortex Reynolds number, a dimensionless group that combines the viscous Reynolds number, swirl number, and the chamber aspect ratio. On the one hand, in the limiting case of $V \rightarrow 0$, the absence of a mean inflow velocity causes the solution to categorically vanish. On the other hand, we can see from Fig. 4b that as the vortex Reynolds number increases, the viscous layer narrows, and the solution shifts toward its inviscid form. Mathematically, this observation can be rigorously confirmed by setting $V \rightarrow \infty$ in Eq. (15) and identically recovering the inviscid solution.

B. Radial Velocity Profile

It may be instructive to recall that the equation from which the wall correction is derived for the radial velocity is arrived at by keeping second order terms. We therefore expect very small deviations from the original inviscid solution. Our hypothesis is confirmed in Fig. 4c where the inviscid solution is gradually regained at a relatively small distance from the wall. Of course, this observation correlates well with the idea that viscous effects are secondary in nature. Note that as the vortex Reynolds number increases, the inviscid solution becomes nearly valid over the entire domain. Viscous effects are seen to promote smoothing of the radial profile, causing both the velocity and its derivative to vanish at the wall. This behavior will have a direct bearing on the shear stresses and, ultimately, on the potential for roll torques.

C. Axial and Radial Boundary Layers

A closed-form expression can be derived for the boundary layer thickness by stating that the boundary layer, δ , is the distance required for the viscous solution to reach 99% of its outer, inviscid form. This classic definition of the boundary layer applies equally well in the axial and radial directions. As one would expect, it leads to explicit solutions that are dependent on the vortex Reynolds number. Thus, after locating the radial position corresponding to the edge of the wall region, this distance may be subtracted from the radius of the chamber to extract the actual thickness of the wall layer. Repeating this analysis in both directions yields:

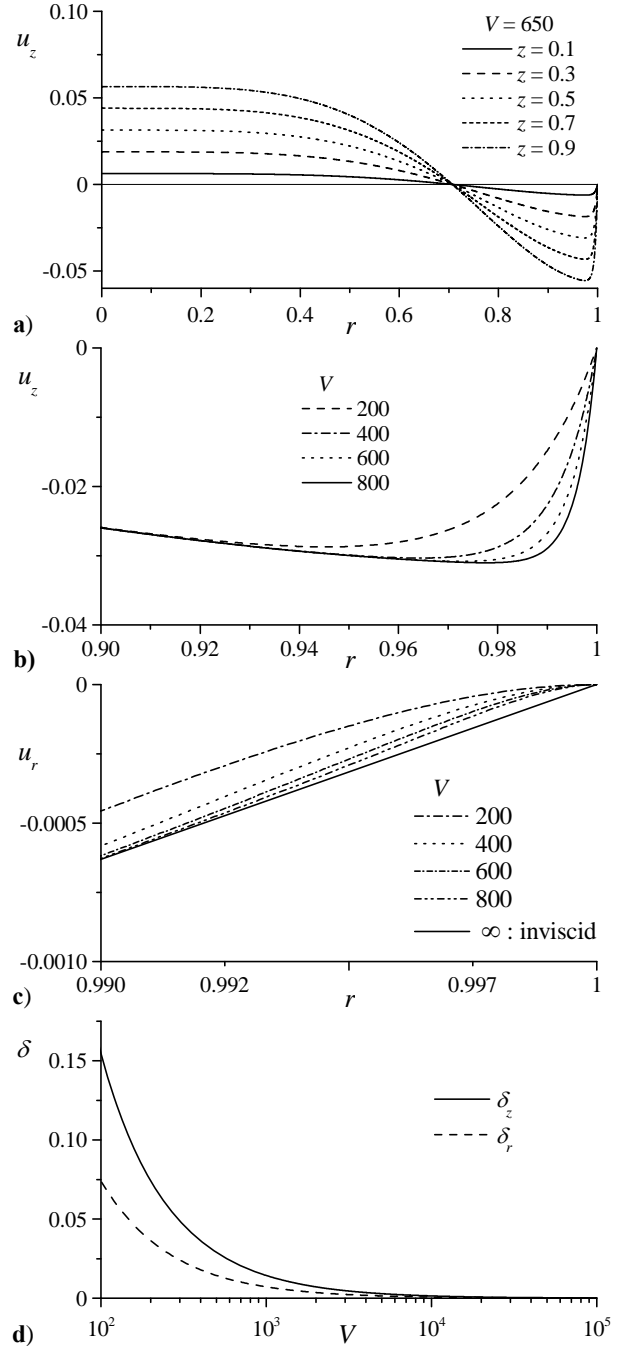


Figure 4. Effects of wall friction: a) axial velocity component at several axial positions and $V = 650$; b) magnified sidewall region for better depiction of axial boundary layer behavior and $z = 0.3$; c) radial velocity profile shown near the sidewall at several values of V ; and d) boundary layer thicknesses as a function of V .

$$\begin{cases} \delta_z = 1 - \sqrt{1 + \frac{4\ln(0.01)}{\alpha V}} \approx 1 - \sqrt{1 - \frac{28.562}{V}} \approx \frac{14.281}{V} \left(1 + \frac{7.1405}{V} + \dots\right) \\ \delta_r = 1 - \sqrt{1 + \frac{2\ln(0.01)}{\alpha V}} \approx 1 - \sqrt{1 - \frac{14.281}{V}} \approx \frac{7.1405}{V} \left(1 + \frac{3.5703}{V} + \dots\right) \end{cases} \quad (27)$$

A one term approximation in Eq. (27) will accrue an error of less than 1% when $V > 722$. Figure 4d shows the effect of increasing the vortex Reynolds number on both axial and radial boundary layer thicknesses. Note that as the vortex Reynolds number increases, the boundary layer thickness conversely diminishes. Eventually, as confirmed through Eq. (27), the thickness becomes inversely proportional to V . Then as δ_z and δ_r tend to zero, the inviscid solution re-emerges.

To verify our scaling analysis, we choose to generate values for κ and ε and compare the calculated boundary layer thickness to the thickness granted by the distinguished limit. With values of $\kappa = 10^{-2}$ and $\varepsilon = 10^{-4}$, the calculated vortex Reynolds number is found to be 628.3, with the thickness at $\delta_z = 0.0230$ and $\delta_r = 0.0114$. The distinguished limit predicts $\delta = \varepsilon / \kappa = 0.01$, which is of the same order as the boundary layer region. Also note that as $V \rightarrow \infty$, $\delta_r \rightarrow \delta_z / 2$. Practically, the radial layer quickly becomes half of the axial layer as the vortex Reynolds number is increased. Compared to the tangential core and wall boundary layers, δ_c and δ_w , obtained by Vyas and Majdalani,²⁵ we have $\delta_c \approx 2.24181/V^{1/2}$ and $\delta_w = \delta_z$. At the outset, one can put

$$\begin{cases} \frac{\delta_z}{\delta_c} = \frac{\delta_w}{\delta_c} \approx 0.446068\sqrt{V} \left(1 - \sqrt{1 - \frac{28.562}{V}}\right) \approx \frac{6.3703}{\sqrt{V}} \left(1 + \frac{7.1405}{V} + \dots\right) \\ \frac{\delta_r}{\delta_c} = \frac{\delta_w}{\delta_c} \approx 0.446068\sqrt{V} \left(1 - \sqrt{1 - \frac{14.281}{V}}\right) \approx \frac{3.1852}{\sqrt{V}} \left(1 + \frac{3.5703}{V} + \dots\right) \end{cases}; V > 49 \quad (28)$$

A comparison between the boundary layers is given in Table 1. At first glance, the equality between axial and tangential boundary layers may appear paradoxical. The unsuspecting analyst may anticipate a steady Prandtl layer to grow in the streamwise direction. However, when recalling that the axial pressure gradient is negligible and that the dominant radial pressure gradient acts uniformly along the length of the chamber, the constant thickness of the tangential boundary layer is no longer surprising. If the sidewall could be likened to an ironing board and the boundary layer envelope to a thin blanket, then the axisymmetric radial pressure would play the role of the iron: it would press the layer evenly against the circumferential wall. Mathematically, it can be seen that the boundary layer equations are similar in both tangential and axial directions. Specifically, both equations are axially independent and exhibit a distinguished limit that balances viscous diffusion and radial convection due to the outflow velocity at the edge of the layer (see Fig. 3). This balance supports the notion that both boundary layers must be of common order.

In hindsight, an even better explanation could be offered. By rethinking this problem, the requirement for the axial boundary layer to match its tangential counterpart could have been deduced from physical arguments alone, without the need for analysis. The reason is this. Because the tangential boundary layer is axially invariant (a byproduct of axisymmetry and an essentially inviscid outer solution), its thickness δ_w remains constant at any position inside the chamber. This feature is illustrated in Fig. 5 where several circular strips, representing the envelope of δ_w , are graphically displayed at three axial stations. Since the axial boundary layer prescribes the thickness of the envelope in the longitudinal direction (thin dashed lines in Fig. 5), it must also remain constant to prevent any axial increase in δ_w . As both boundary layers are orthogonal, any increase in δ_z cannot be realized without affecting the size of δ_w . In a way, the asymptotic derivation presented above is fully justified because any other outcome would have been in violation of the basic assumptions associated with our model. As a windfall, the dismissal of the axial pressure gradient in the asymptotic treatment is reconfirmed.

It may be helpful to note another perspective on this problem that may be gained from examining the

Table 1. Comparison of axial, radial, core and tangential boundary layers at several values of V

| V | δ_z | δ_r | δ_c^* | δ_w^* |
|------|------------|------------|--------------|--------------|
| 200 | 0.07415 | 0.03636 | 0.15852 | 0.07415 |
| 400 | 0.03636 | 0.01801 | 0.11209 | 0.03636 |
| 600 | 0.02409 | 0.01197 | 0.09152 | 0.02409 |
| 800 | 0.01801 | 0.00896 | 0.07926 | 0.01801 |
| 1000 | 0.01438 | 0.00716 | 0.07089 | 0.01438 |

*Vyas and Majdalani²⁵

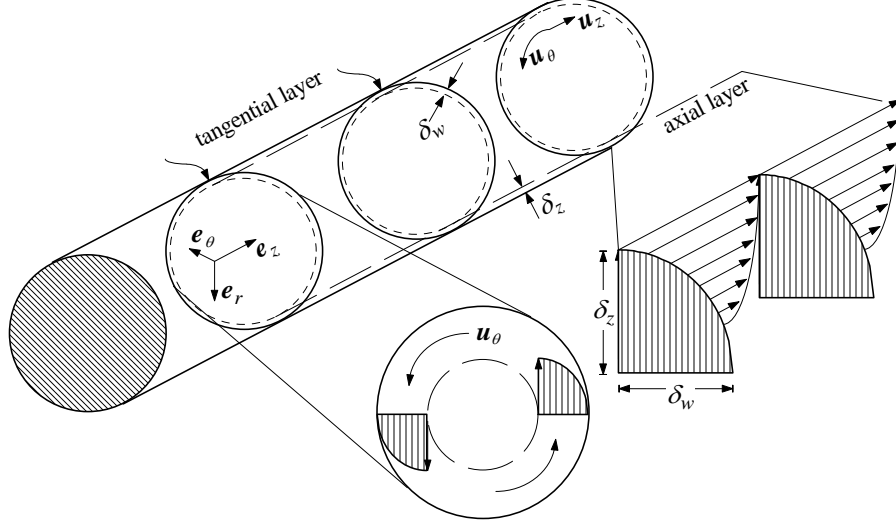


Figure 5. Axial invariance of the tangential and axial boundary layers.

resultant velocity and its impact on the flow motion. Given that fluid particles only sense the resultant velocity \mathbf{u} (i.e., the individual components (u_r, u_θ, u_z) are mere orthogonal projections), it may be safely argued that the resultant boundary layer is directly controlled by \mathbf{u} . At the outset, the composite layer is seen to be dominated by the swirl velocity, given that $\mathbf{u} = \mathbf{u}_\theta + \mathcal{O}(\kappa)$. The actual boundary layer forming above the surface, which is the byproduct of the axial and tangential layers, must therefore conform to the flow being swirl driven. It will consist of an axisymmetric layer spiraling around and climbing the short chamber height without experiencing any appreciable growth or depreciation.

D. Shear Stress Tensor

The wall shear stress obtained by Vyas and Majdalani²⁵ can be evaluated in view of the updated equations. One finds

$$\begin{aligned} \tau_{rr} &= 2\varepsilon \frac{\partial u_r}{\partial r} = \varepsilon^2 V \left\{ \frac{\sin(\pi r^2)}{\pi r^2} \left[1 - e^{-\frac{1}{2}\alpha V(1-r^2)} \right] + \frac{\alpha}{\pi} V \sin(\pi r^2) e^{-\frac{1}{2}\alpha V(1-r^2)} - 2 \cos(\pi r^2) \left[1 - e^{-\frac{1}{2}\alpha V(1-r^2)} \right] \right\} \\ &= 2\pi\varepsilon\kappa \left\{ \frac{\alpha}{\pi} V \sin(\pi r^2) e^{-\frac{1}{2}\alpha V(1-r^2)} + \left[\frac{\sin(\pi r^2)}{\pi r^2} - 2 \cos(\pi r^2) \right] \left[1 - e^{-\frac{1}{2}\alpha V(1-r^2)} \right] \right\} \end{aligned} \quad (29)$$

$$\tau_{\theta\theta} = 2\varepsilon \left(\frac{1}{r} \frac{\partial u_\theta}{\partial \theta} + \frac{u_r}{r} \right) = -\frac{\varepsilon^2 V}{\pi r^2} \sin(\pi r^2) \left[1 - e^{-\frac{1}{2}\alpha V(1-r^2)} \right] = -\frac{2\varepsilon\kappa}{r^2} \sin(\pi r^2) \left[1 - e^{-\frac{1}{2}\alpha V(1-r^2)} \right] \quad (30)$$

$$\tau_{zz} = 2\varepsilon \frac{\partial u_z}{\partial z} = 2\varepsilon^2 V \cos(\pi r^2) \left[1 - e^{-\frac{1}{4}\alpha V(1-r^2)} \right] = 4\pi\varepsilon\kappa \cos(\pi r^2) \left[1 - e^{-\frac{1}{4}\alpha V(1-r^2)} \right] \quad (31)$$

$$\begin{aligned} \tau_{r\theta} &= \varepsilon \left[\frac{1}{r} \frac{\partial u_r}{\partial \theta} + r \frac{\partial}{\partial r} \left(\frac{u_\theta}{r} \right) \right] = \frac{\varepsilon}{2r^2} \left[\frac{(4+r^2V)e^{-\frac{1}{4}Vr^2}}{1-e^{-\frac{1}{4}V}} + \frac{[4-r^2V(\frac{1}{6}\pi^2-1)]e^{-\frac{1}{4}\alpha V(1-r^2)} - 2 - 2e^{-\frac{1}{4}\alpha V}}{1-e^{-\frac{1}{4}\alpha V}} - 2 \coth\left(\frac{V}{8}\right) \right] \\ &\approx \frac{\varepsilon}{2r^2} \left[(4+Vr^2)e^{-\frac{1}{4}Vr^2} + (4-\alpha Vr^2)e^{-\frac{1}{4}\alpha V(1-r^2)} - 4 \right] \quad (\text{with no transcendental parts}) \end{aligned} \quad (32)$$

$$\tau_{\theta z} = \varepsilon \left(\frac{1}{r} \frac{\partial u_z}{\partial \theta} + \frac{\partial u_\theta}{\partial z} \right) = 0 \quad (33)$$

$$\begin{aligned}\tau_{zr} &= \varepsilon \left(\frac{\partial u_z}{\partial r} + \frac{\partial u_r}{\partial z} \right) = \varepsilon \frac{\partial u_z}{\partial r} = -\frac{1}{2} \varepsilon^2 V r z \left\{ 4\pi \sin(\pi r^2) \left[1 - e^{-\frac{1}{4} \alpha V (1-r^2)} \right] + \alpha V \cos(\pi r^2) e^{-\frac{1}{4} \alpha V (1-r^2)} \right\} \\ &= -\pi \varepsilon \kappa r z \left\{ 4\pi \sin(\pi r^2) \left[1 - e^{-\frac{1}{4} \alpha V (1-r^2)} \right] + \alpha V \cos(\pi r^2) e^{-\frac{1}{4} \alpha V (1-r^2)} \right\}\end{aligned}\quad (34)$$

These are illustrated in Fig. 6. Having fully determined the shear stress tensor, it is possible to evaluate it at the sidewall. This will enable us to predict the roll torques in the vortex chamber by integrating the shear stress over the circumferential wall. By calculating each member in Eqs. (29)-(34) as $r \rightarrow 1$, we collect

$$\begin{cases} \tau_{rr}^{(w)} = \tau_{\theta\theta}^{(w)} = \tau_{zz}^{(w)} = \tau_{\theta z}^{(w)} = 0 \\ \tau_{r\theta}^{(w)} = -\frac{1}{2} \alpha \varepsilon V = -\pi \left(\frac{1}{6} \pi^2 - 1 \right) \kappa \\ \tau_{zr}^{(w)} = \frac{1}{2} \alpha \varepsilon^2 V^2 z = 2 \left(\frac{1}{6} \pi^2 - 1 \right) \pi^2 \kappa^2 z \end{cases}\quad (35)$$

Compared to the original work,²⁵ the new corrections slightly alter the previous prediction for the shear stress at the wall. Essentially, τ_{zz} and τ_{rr} are found to be identically zero, while τ_{zr} reappears with a small value. Using a Pythagorean sum of orthogonal components, the total shear stress may be calculated from

$$\tau_0^{(w)} = \sqrt{\left(\tau_{r\theta}^{(w)} \right)^2 + \left(\tau_{zr}^{(w)} \right)^2} = \pi \alpha \kappa \sqrt{1 + 4\pi^2 \kappa^2 z^2} = \frac{1}{2} \alpha \varepsilon V \sqrt{1 + \varepsilon^2 V^2 z^2}\quad (36)$$

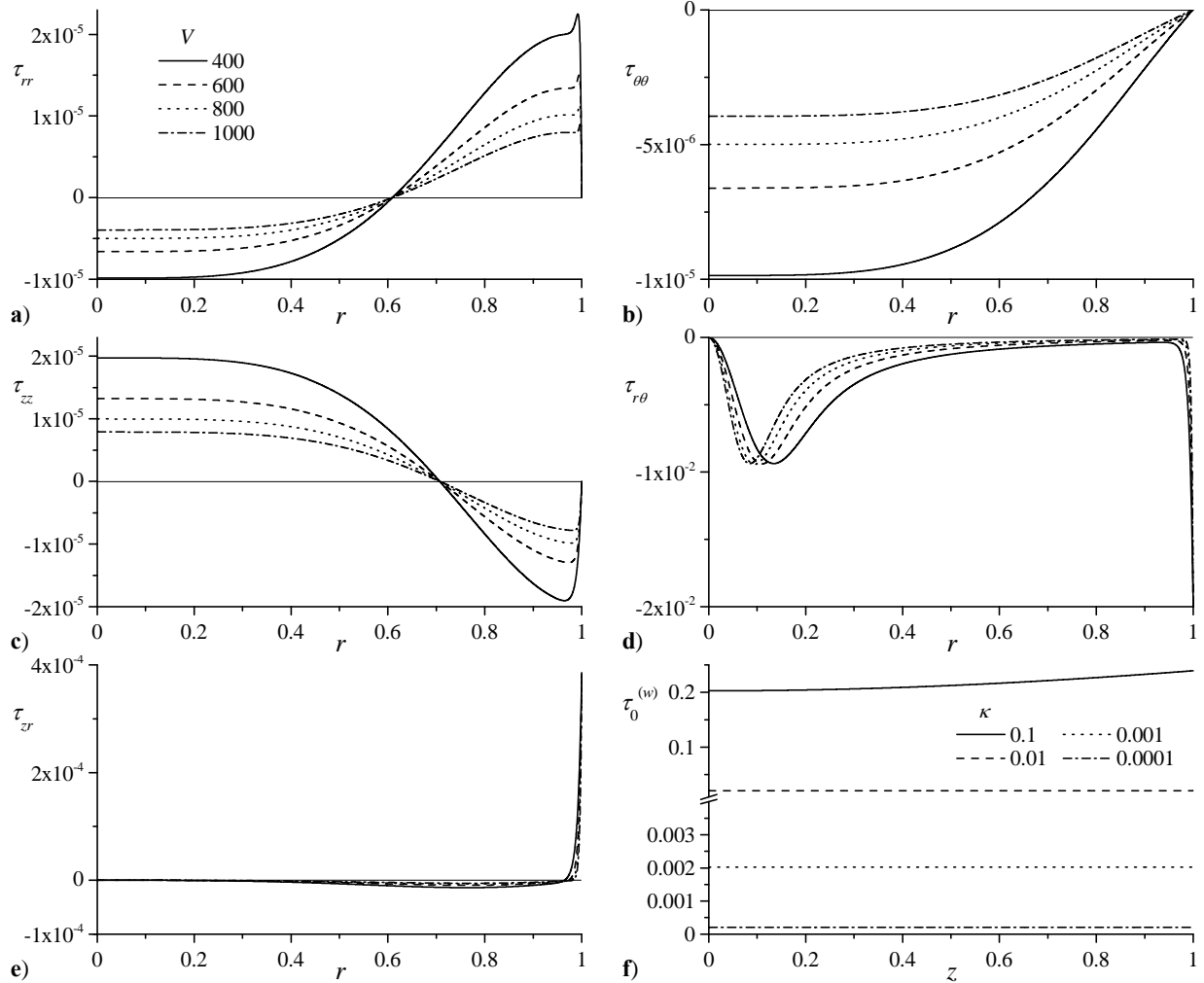


Figure 6. Shear stresses at several values of V , $z = 0.3$ and $\kappa = 0.01$: a) τ_{rr} , b) $\tau_{\theta\theta}$, c) τ_{zz} , d) $\tau_{r\theta}$, e) τ_{zr} , and f) $\tau_0^{(w)}$. In part f, κ is varied by three orders of magnitude as indicated.

By carefully examining Figs. 6a-f, it may be seen that the flow is still dominated by the shear component $\tau_{r\theta}$, which is an order of magnitude larger than τ_{zr} . The total shear force for given values of κ can be determined by integrating the shear stress over the entire lateral surface of the chamber. One gets

$$\begin{aligned} F_0^{(w)} &= \pi\alpha\kappa \int_0^{2\pi} \int_0^l \sqrt{1+(\varepsilon zV)^2} dz d\theta = 2\pi^2\alpha\kappa \int_0^l \sqrt{1+(\varepsilon zV)^2} dz = \pi^2\alpha\kappa l \left[\sqrt{1+(\varepsilon lV)^2} + \frac{\sinh^{-1}(\varepsilon lV)}{\varepsilon lV} \right] \\ &= \frac{1}{2}\pi\alpha(2\pi\kappa l) \left[\sqrt{1+(2\pi\kappa l)^2} + \frac{\sinh^{-1}(2\pi\kappa l)}{2\pi\kappa l} \right] = \frac{\pi\alpha}{2\sigma^2} \left[\sqrt{1+\sigma^2} + \sigma^2 \sinh^{-1}(\sigma^{-1}) \right] \\ &= \pi\alpha Q_i \left(1 + \frac{1}{6}Q_i^2 - \frac{1}{40}Q_i^4 + \frac{1}{112}Q_i^6 - \frac{5}{11152}Q_i^8 + \dots \right) \end{aligned} \quad (37)$$

Thus, given a chamber of unit radius, the normalized tangential shear force will be the same as the roll torque T_θ acting on the inner wall. When written in dimensional form, the torque may be expressed as

$$\bar{T}_\theta = \pi\alpha Q_i \rho U^2 a^3 = \left(\frac{1}{6}\pi^3 - \pi\right) \rho \bar{Q}_i U a = 2.02612 \dot{m}_i U a = 1.01306 \dot{m}_i U D ; \quad D = 2a \quad (38)$$

Note that the torque exerted by the fluid on the wall acts in the same direction as the tangential velocity at entry. It is directly proportional to the mass flow rate \dot{m}_i , circumferential injection velocity U , and chamber diameter D . Recalling that $\bar{F}_M = \dot{m}_i U$ represents the fluid momentum force according to control-volume theory, the actual torque is nearly equal to the injection moment couple, namely, the product of \bar{F}_M and the chamber diameter D .

E. Pressure Distribution

The pressure is evaluated with the latest viscous corrections at hand. Based on Euler's equations, we obtain a leading order solution from

$$\frac{\partial p}{\partial r} = \frac{u_\theta^2}{r} - u_r \frac{\partial u_r}{\partial r} - u_z \frac{\partial u_r}{\partial z} \quad (39)$$

Injecting the improved representations for the velocity components, we thereby retrieve

$$\begin{aligned} \frac{\partial p}{\partial r} &= \kappa^2 r^{-1} \sin(\pi r^2) \left[1 - e^{-\frac{1}{2}\alpha V(1-r^2)} \right] \left\{ \left[r^{-2} \sin(\pi r^2) - 2\pi \cos(\pi r^2) \right] \left[1 - e^{-\frac{1}{2}\alpha V(1-r^2)} \right] + \alpha V \sin(\pi r^2) e^{-\frac{1}{2}\alpha V(1-r^2)} \right\} \\ &\quad + \frac{1}{r^3} \left[\frac{1 - e^{-\frac{1}{4}Vr^2}}{1 - e^{-\frac{1}{4}V}} + \frac{1 - e^{-\frac{1}{4}\alpha V(1-r^2)}}{1 - e^{-\frac{1}{4}\alpha V}} - 1 \right]^2 \end{aligned} \quad (40)$$

Equation (40) may be carefully simplified and collapsed into

$$\frac{\partial p}{\partial r} \approx \frac{1}{r^3} \left[1 - e^{-\frac{1}{4}Vr^2} - e^{-\frac{1}{4}\alpha V(1-r^2)} \right]^2 \quad (41)$$

As for the axial gradient, it can be similarly obtained from

$$\frac{\partial p}{\partial z} = -u_r \frac{\partial u_z}{\partial r} - u_z \frac{\partial u_z}{\partial z} \quad (42)$$

At the onset of this calculation, it may be realized that the axial gradient is of order κ^2 . One may also recall that radial terms of order κ^2 have been discounted elsewhere. To remain asymptotically consistent with the truncation order incurred in this model, the axial gradient is hereby dismissed. It may be easily shown that its retention is immaterial. Instead, we are now able to retrieve the pressure directly from Eq. (41).

With the help of symbolic software,³¹ Eq. (41) may be integrated and anchored to a constant reference pressure at the wall, $p_0 = p(1)$. The result is

$$\begin{aligned} p &= p_0 - \frac{1}{2r^2} \left\{ \left(1 - e^{-\frac{1}{4}Vr^2} \right)^2 + \left[1 - e^{-\frac{1}{4}\alpha V(1-r^2)} \right]^2 - 1 + 2e^{-\frac{1}{4}V} \left[\alpha + (1-\alpha)r^2 \right] \right\} \\ &\quad - \frac{V}{4} \left\{ \text{Ei}\left(-\frac{1}{2}Vr^2\right) - \text{Ei}\left(-\frac{1}{4}Vr^2\right) + \alpha e^{-\frac{1}{4}\alpha V} \left[\text{Ei}\left(\frac{1}{4}\alpha Vr^2\right) - \text{Ei}\left(\frac{1}{4}\alpha V\right) \right] - \alpha e^{-\frac{1}{2}\alpha V} \left[\text{Ei}\left(\frac{1}{2}\alpha Vr^2\right) - \text{Ei}\left(\frac{1}{2}\alpha V\right) \right] \right\} \end{aligned} \quad (43)$$

where $\text{Ei}(x)$ denotes the second exponential integral function,

$$\text{Ei}(x) = \gamma + \ln|x| + \sum_{m=1}^{\infty} \frac{x^m}{m!m}; \quad \gamma = 0.5772156649 \quad (\text{Euler's constant}) \quad (44)$$

Note that when Eq. (43) is compared to its precursor obtained in,²⁵ an additional term appears that may be attributed to the influence of the axial boundary layer. This term is $-r^{-2} \exp\left\{-\frac{1}{4}V\left[\alpha + (1-\alpha)r^2\right]\right\}$. Nonetheless, when the pressure is plotted in Fig. 7, the influence of this term is found to be very small. The axial and radial corrections for the pressure are therefore inconsequential.

F. Vorticity and Circulation

Vorticity

The axisymmetric vorticity is given by

$$\begin{aligned} \mathbf{\Omega} &= -\frac{\partial u_{\theta}}{\partial z} \mathbf{e}_r + \left(\frac{\partial u_r}{\partial z} - \frac{\partial u_z}{\partial r}\right) \mathbf{e}_{\theta} + \left(\frac{\partial u_{\theta}}{\partial r} + \frac{u_{\theta}}{r}\right) \mathbf{e}_z \\ &= \pi r z \kappa \left\{ \alpha V e^{-\frac{1}{4}\alpha V(1-r^2)} \cos(\pi r^2) + 4\pi \left[1 - e^{-\frac{1}{4}\alpha V(1-r^2)}\right] \sin(\pi r^2) \right\} \mathbf{e}_{\theta} + \frac{V}{2} \left[\frac{e^{-\frac{1}{4}Vr^2}}{1 - e^{-\frac{1}{4}V}} - \frac{\alpha e^{-\frac{1}{4}\alpha V(1-r^2)}}{1 - e^{-\frac{1}{4}\alpha V}} \right] \mathbf{e}_z \end{aligned} \quad (45)$$

In the classical Rankine vortex,¹ a piecewise solution is posited in which the rotational core is governed by solid body rotation, and the irrotational tail is derivable from a scalar potential. Obviously, no vorticity can originate from the tail, especially in an unbounded domain. In the confined bidirectional vortex flowfield, a section of the free vortex segment resembles that of Rankine's and as such, remains vorticity free. Axial vorticity is only recovered in the presence of the wall and the core as seen in Fig. 8. In fact we find the influence of axial and radial boundary layers on vorticity production to be small. The expression that we arrive at is identical to that of Vyas and Majdalani,²⁵ particularly

$$\Omega_z \approx \frac{1}{2}V \left[e^{-\frac{1}{4}Vr^2} - \alpha e^{-\frac{1}{4}\alpha V(1-r^2)} \right] \quad (46)$$

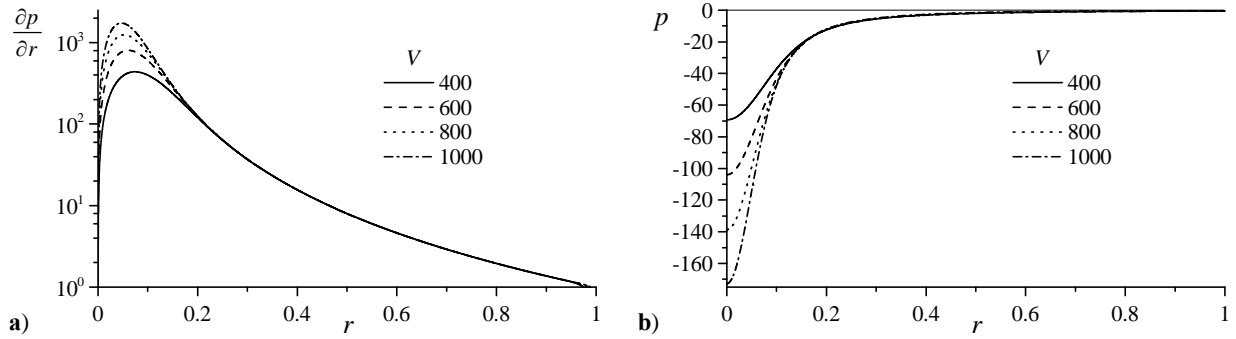


Figure 7. Variation of the radial pressure gradient and pressure at four values of V .

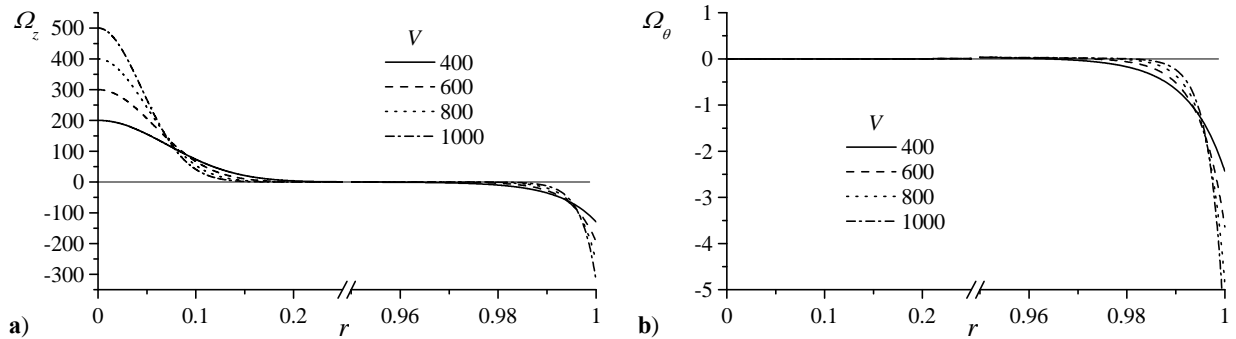


Figure 8. Sidewall and near-core behavior of a) axial and b) tangential vorticities ($\kappa = 0.01, z = 3$) at four values of V .

The tangential vorticity Ω_θ is of order κ and is hence small in comparison to the axial component. This behavior reinforces the character of the flowfield as being fundamentally swirl dominated. However, while the tangential vorticity is approximately zero throughout the majority of the chamber, its contribution becomes appreciable in the sidewall region.

Circulation

The circulation Γ is defined as the line integral of the tangential component of the velocity around a closed curve. It can be directly related to the vorticity through the Stokes theorem, namely,

$$\Gamma = \iint_A (\nabla \times \mathbf{u}) \cdot \mathbf{n} dA \quad (47)$$

In simple terms, Γ is the axial component of vorticity integrated over the circular cross-sectional area of the chamber A . In our case, this operation translates into

$$\Gamma = \frac{1}{2} V \int_0^{2\pi} \int_0^1 \left[\frac{e^{-\frac{1}{4}Vr^2}}{1 - e^{-\frac{1}{4}V}} - \frac{\alpha e^{-\frac{1}{4}\alpha V(1-r^2)}}{1 - e^{-\frac{1}{4}\alpha V}} \right] r dr d\theta = 0 \quad (48)$$

Note that the integral vanishes identically. Upon further scrutiny, one identifies a one-to-one cancellation of the vorticity products in the core region with those in the boundary layer region. For external flows, as is the case in the majority of classical vortex models that exhibit a singularity at the core, a finite circulation is obtained when the singular point is included in the domain of integration.

G. Swirling Intensity

As a predictor of mixing potential with respect to various configurations we evaluate the swirling intensity according to Chang and Dhir³² and apply it to the bidirectional vortex as performed by Vyas, Majdalani and Chiaverini.²² We find

$$\tilde{\Omega} = \frac{\int_0^{1/\sqrt{2}} u_z u_\theta r dr}{4 \left(\int_0^{1/\sqrt{2}} u_z r dr \right)^2} \quad (49)$$

At this juncture, symbolic programming may be readily used to evaluate $\tilde{\Omega}$; we get

$$\tilde{\Omega} = -\frac{\pi\sqrt{\pi}(1-i)}{4\sqrt{2}} \frac{1}{\kappa z} \left\{ \frac{\operatorname{erf} \left[\frac{1}{4}(1+i)\sqrt{4\pi-iV} \right]}{\sqrt{4\pi-iV}} + \frac{\operatorname{erfi} \left[\frac{1}{4}(1+i)\sqrt{4\pi+iV} \right]}{\sqrt{4\pi+iV}} - \frac{(1+i)}{\sqrt{\pi}} C(1) \right\} \quad (50)$$

which is true for $V > 49$; here $C(1) = 0.779893$ where $C(x)$ is the Fresnel integral defined as

$$C(x) = \int_0^x \cos\left(\frac{1}{2}\pi r^2\right) dr \quad (51)$$

Equation (50) provides an accurate and compact expression for the swirling intensity. Notice that as the vortex Reynolds number becomes very large, the swirling intensity approaches an asymptotic value given by

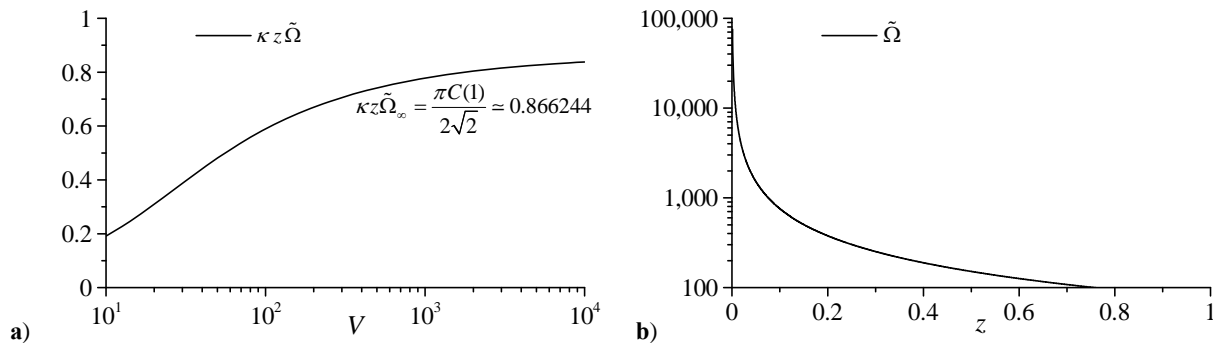


Figure 9. Variation of swirling intensity with a) the vortex Reynolds number and b) the axial distance from the headwall. The latter is given for $\kappa = 0.01$ and $V = 650$.

$$\tilde{\Omega}_\infty \approx \frac{\pi C(1)}{2\sqrt{2}} \frac{1}{\kappa z} = \frac{0.866244}{\kappa z} \quad (52)$$

This can be inferred graphically from Fig. 9. Note that Eq. (50) is identical to the one found by Vyas and Majdalani.²⁵ We conclude that the axial and radial boundary layers have a secondary impact on $\tilde{\Omega}$.

IV. Conclusions

This study extends our analytical treatment of the bidirectional vortex which, since inception, has relied on solutions obtained directly from first principles. Both axial and radial boundary layers at the sidewall, which have been dismissed in previous analyses, are accounted for and resolved. While the axial boundary layer is required to bring the parallel component of the velocity to observe the no-slip condition, the radial layer is formed to prevent the abrupt clipping of the radial velocity at the sidewall. The work parallels the analysis of the wall-tangential boundary layer that has resulted in a rectified form of the swirl velocity. Using similar perturbation tools, the theory of matched-asymptotic expansions is applied to capture the small viscous effects at the confining boundary. Additionally here, both independent and *dependent* variables have to be transformed, lest an intractable problem is obtained. In the tangential direction, a simple boundary condition is imposed on the conserved angular momentum in the far-field, namely, a pure constant corresponding to a free vortex, i.e., $(ru_\theta) = 1$. Presently, the outer solution corresponds to sinusoidal functions of at least one variable. Thus, after several transformations, expansions, and asymptotic reductions, uniformly valid approximations are derived for both axial and radial velocities. The viscous corrections are found to mirror those constructed previously in the tangential direction. Their role here is to cause the axial velocity to vanish at the sidewall while providing a measure of tempering to the radial profile, causing it to terminate smoothly. We note that in the process of establishing the inner equations that control the rapid changes in the vicinity of the wall, expressions are obtained that resemble those appropriate for two-dimensional boundary layer analysis.

In light of the new corrections, several key characteristics of the bidirectional vortex are quantified. Theoretical thicknesses for the axial and radial layers are extracted, and these are compared to both wall-tangential and core boundary layers. The axial boundary layer δ_z is found to be generally twice as large as the radial layer δ_r but of equal size to the tangential layer δ_w obtained by Vyas and Majdalani.²⁵ These layers are inversely proportional to the vortex Reynolds number to the extent of increasing with the viscosity, aspect ratio, and swirl number. By the same token, they become thinner with successive increases in the circumferential velocity.

The equality between axial and tangential boundary layers, which may be surprising at first, may be physically anticipated without the need for asymptotic analysis. Given that the resultant velocity is nearly equal to the tangential velocity, the boundary layer thickness is dominated by its tangential component. Moreover, the tangential boundary layer remains invariant in the axial direction to the extent that its thickness measured along the length of the chamber can only be identical to its thickness measured along the circumference. The equality $\delta_z = \delta_w$ is thus a byproduct of axisymmetry and the invariance of the swirl velocity and pressure in the axial direction.

With respect to the shear stresses, the axial and radial corrections help to refine the stress tensor in several of its elements. The $\tau_{zr}^{(w)}$ term and, hence, the total shear are seen to exhibit a small axial dependence which cannot be manifested in the absence of friction parallel to the wall. We also determine that $\tau_{rr}^{(w)}$ and $\tau_{zz}^{(w)}$ are not asymptotically small but strictly zero. Overall, only secondary contributions to the resultant shear force are realized. The total roll torque remains dominated by the tangential component. Its dimensional form is evaluated and found to depend on the fluid moment couple, a product of the mass flow rate into the chamber, the circumferential velocity, and the chamber diameter. It is interesting that the differential analysis leads to a similar prediction of torque as that obtained from a global, control-volume approach.

When evaluating the pressure gradient, it may be remarked that the prevailing terms are those connected with the swirl velocity. Physically, terms referring to axial and radial velocities or their derivatives are negligible as they tend to be of order κ^2 . At length, we recover nearly the same asymptotic form derived by Vyas and Majdalani.²⁵ As for the axial pressure gradient, we find all of its terms to be of order κ^2 . In the spirit of asymptotic consistency, the axial pressure dependence is ignored. Qualitatively, a much lower pressure is captured throughout the core in comparison to the wall region. This suction pressure is responsible for attracting the flow inwardly, causing the fluid in the outer annular vortex to negotiate a 180 degree turn near the headwall before pouring into the inner vortex funnel. It is also responsible, in part, for the constant cross flow that persists along the length of the mantle, causing the annular fluid to spill inwardly.

With respect to vorticity, the parallelism with the Rankine vortex continues to hold to some extent. Here too vorticity is confined to the viscous core or sidewall regions. We also continue to see vorticity dominated by its axial component and, along with other essential flow features, to be strongly dependent on V . Interestingly, circulation in the presence of bidirectional motion is found to be null. This behavior is due to the coexistence and counterbalance between vorticities produced in the core and in the sidewall region. Despite their presence at the far ends of the domain, their contributions simply cancel. This outcome precludes the ability to express the bidirectional vortex in terms of circulation. For the same reason, direct correlations with historical models defined by this parameter are lost.

The swirling intensity continues to be largest near the headwall and mostly dominated by the tangential velocity (Fig. 9). The singularity at the headwall is not resolved in the present model but its treatment is hoped to be achieved in future work. The large swirling intensities encountered near the headwall turn this region into an ideal site for mixing. Such behavior is advantageous to the VCCWC chamber in which the useful attributes of a cyclone are harnessed. By providing an excellent potential for improved mixing between oxidizer and fuel streams, the VCCWC is poised to achieve high efficiency and low-cost operability.

Acknowledgments

The authors are deeply grateful for the support received from ORBITEC (FA8650-05-C-2612) and the National Science Foundation (CMS-0353518).

References

- ¹Rankine, W. J. M., *A Manual of Applied Mechanics*, 9th ed., C. Griffin and Co., London, UK, 1858.
- ²Lamb, H., *Hydrodynamics*, 6th ed., Cambridge University Press, Cambridge, UK, 1932.
- ³Burgers, J. M., "A Mathematical Model Illustrating the Theory of Turbulence," *Advances in Applied Mechanics*, Vol. 1, 1948, pp. 171-196.
- ⁴Batchelor, G. K., "Axial Flow in Trailing Line Vortices," *Journal of Fluid Mechanics*, Vol. 20, No. 4, 1964, pp. 645-658.
- ⁵Penner, S. S., "Elementary Considerations of the Fluid Mechanics of Tornadoes and Hurricanes," *Acta Astronautica*, Vol. 17, 1972, pp. 351-362.
- ⁶Königl, A., "Stellar and Galactic Jets: Theoretical Issues," *Canadian Journal of Physics*, Vol. 64, 1986, pp. 362-368.
- ⁷Kyrala, A., "An Explanation of the Persistence of the Great Red Spot of Jupiter," *Moon and the Planets*, Vol. 26, No. 2, 1982, pp. 105-107.
- ⁸Eloy, C., and Le Dizès, S., "Three-Dimensional Instability of Burgers and Lamb-Oseen Vortices in a Strain Field," *Journal of Fluid Mechanics*, Vol. 378, No. 1, 1999, pp. 145-166.
- ⁹Batterson, J. W., Maicke, B. A., and Majdalani, J., "Advancements in Theoretical Models of Confined Vortex Flowfields," JANNAF Paper TP-2007-222, May 2007.
- ¹⁰Alekseenko, S. V., Kuibin, P. A., Okulov, V. L., and Shtork, S. I., "Helical Vortices in Swirl Flow," *Journal of Fluid Mechanics*, Vol. 382, 1999, pp. 195-243.
- ¹¹Schmid, P. J., and Rossi, M., "Three-Dimensional Stability of a Burgers Vortex," *Journal of Fluid Mechanics*, Vol. 500, No. 1, 2004, pp. 103-112.
- ¹²Olendraru, C., and Sellier, A., "Viscous Effects in the Absolute-Convective Instability of the Batchelor Vortex," *Journal of Fluid Mechanics*, Vol. 459, No. 1, 2002, pp. 371-396.
- ¹³Pérez-Saborid, M., Herrada, M. A., Gómez-Barea, A., and Barrero, A., "Downstream Evolution of Unconfined Vortices: Mechanical and Thermal Aspects," *Journal of Fluid Mechanics*, Vol. 471, No. 1, 2002, pp. 51-70.
- ¹⁴Sullivan, R. D., "A Two-Cell Vortex Solution of the Navier-Stokes Equations," *Journal of the Aerospace Sciences*, 1959, pp. 767-768.
- ¹⁵Vatistas, G. H., Lin, S., and Kwok, C. K., "Theoretical and Experimental Studies on Vortex Chamber Flows," *AIAA Journal*, Vol. 24, No. 4, 1986, pp. 635-642.
- ¹⁶Vatistas, G. H., Lin, S., and Kwok, C. K., "Reverse Flow Radius in Vortex Chambers," *AIAA Journal*, Vol. 24, No. 11, 1986, pp. 1872-1873.
- ¹⁷Vatistas, G. H., Jawarneh, A. M., and Hong, H., "Flow Characteristics in a Vortex Chamber," *The Canadian Journal of Chemical Engineering*, Vol. 83, No. 6, 2005, pp. 425-436.
- ¹⁸Bloor, M. I. G., and Ingham, D. B., "The Flow in Industrial Cyclones," *Journal of Fluid Mechanics*, Vol. 178, 1987, pp. 507-519.
- ¹⁹Chiaverini, M. J., Malecki, M. J., Sauer, J. A., and Knuth, W. H., "Vortex Combustion Chamber Development for Future Liquid Rocket Engine Applications," AIAA Paper 2002-2149, July 2002.
- ²⁰Chiaverini, M. J., Malecki, M. J., Sauer, J. A., Knuth, W. H., and Majdalani, J., "Vortex Thrust Chamber Testing and Analysis for O₂-H₂ Propulsion Applications," AIAA Paper 2003-4473, July 2003.
- ²¹Chiaverini, M. J., Malecki, M. M., Sauer, J. A., Knuth, W. H., and Hall, C. D., "Testing and Evaluation of Vortex Combustion Chamber for Liquid Rocket Engines," JANNAF, 2002.

- ²²Vyas, A. B., Majdalani, J., and Chiaverini, M. J., "The Bidirectional Vortex. Part 1: An Exact Inviscid Solution," AIAA Paper 2003-5052, July 2003.
- ²³Majdalani, J., and Rienstra, S. W., "On the Bidirectional Vortex and Other Similarity Solutions in Spherical Coordinates," *Journal of Applied Mathematics and Physics (ZAMP)*, Vol. 58, No. 2, 2007, pp. 289-308.
- ²⁴Vyas, A. B., Majdalani, J., and Chiaverini, M. J., "The Bidirectional Vortex. Part 2: Viscous Core Corrections," AIAA Paper 2003-5053, July 2003.
- ²⁵Vyas, A. B., and Majdalani, J., "Characterization of the Tangential Boundary Layers in the Bidirectional Vortex Thrust Chamber," AIAA Paper 2006-4888, July 2006.
- ²⁶Prandtl, L., "Zur Berechnung Der Grenzschichten," *Journal of Applied Mathematics and Mechanics*, Vol. 18, 1938, pp. 77-82.
- ²⁷Conlisk, A. T., "Source-Sink Flows in a Rapidly Rotating Annulus," Ph.D. Dissertation, Purdue University, 1978.
- ²⁸Tetervin, N., "Boundary-Layer Momentum Equations for Three-Dimensional Flow," National Advisory Committee for Aeronautics, NACA Rept., Langley Field, VA, November 17 1947.
- ²⁹Culick, F. E. C., "Rotational Axisymmetric Mean Flow and Damping of Acoustic Waves in a Solid Propellant Rocket," *AIAA Journal*, Vol. 4, No. 8, 1966, pp. 1462-1464.
- ³⁰Majdalani, J., and Saad, T., "The Taylor-Culick Profile with Arbitrary Headwall Injection," *Physics of Fluids*, Vol. 19, No. 6, 2007.
- ³¹Wolfram, S., *Mathematica. A System for Doing Mathematics on Computer*. Addison Wesley, Reading, MA, 1988.
- ³²Chang, F., and Dhir, V. K., "Mechanisms of Heat Transfer Enhancement and Slow Decay of Swirl in Tubes with Tangential Injection," *International Journal of Heat and Fluid Flow*, Vol. 16, No. 2, 1995, pp. 78-87.